

See discussions, stats, and author profiles for this publication at: <https://www.researchgate.net/publication/251383264>

Multiaxial stress state assessed by 3D X-Ray tomography on semi crystalline

ARTICLE · JUNE 2011

DOI: 10.1007/978-1-4614-0228-2_7

READS

34

3 AUTHORS:



[L. Laiarinandrasana](#)

MINES ParisTech

72 PUBLICATIONS 441 CITATIONS

SEE PROFILE



[T. F. Morgeneyer](#)

MINES ParisTech

56 PUBLICATIONS 362 CITATIONS

SEE PROFILE



[Henry Proudhon](#)

MINES ParisTech

87 PUBLICATIONS 547 CITATIONS

SEE PROFILE

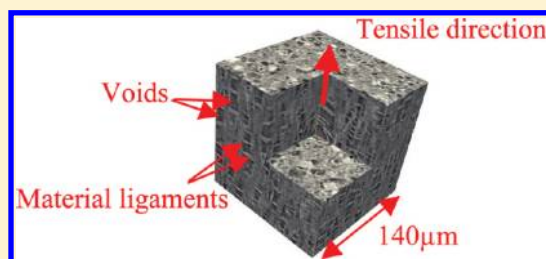
Effect of Multiaxial Stress State on Morphology and Spatial Distribution of Voids in Deformed Semicrystalline Polymer Assessed by X-ray Tomography

Lucien Laiarinandrasana,* Thilo F. Morgeneyer,[†] Henry Proudhon,[†] Franck N'guyen,[†] and Eric Maire[‡]

[†]MINES Paristech, Centre des Matériaux - CNRS UMR 7633, BP 87, 91003 Evry Cedex, France

[‡]INSA-Lyon, MATEIS CNRS UMR5510, Université de Lyon, 7 Avenue Jean Capelle, 69621 Villeurbanne, France

ABSTRACT: Cavitation in the semicrystalline polymer polyamide 6 has been studied in terms of 3D void morphology and distribution in the notched region of axisymmetric specimens using synchrotron radiation tomography at submicrometer resolution. Ex-situ (interrupted and unloaded) tests at different stages of straining reveal damage initiation in form of penny-shaped crazes at maximum load. An in-situ (under load) test confirms the damage morphology at maximum load. When a neck appears and extends within the notch, the penny-shaped crazes extend in height, resulting in a volume change. Final failure is seen to occur from the specimen interior via coalescence of several voids resulting in large cavities. The multiaxial stress state generated by the axisymmetric notch causes crazes/cracks that are larger in diameter than those occurring during necking of an initially smooth specimen. The distribution void volume fraction as a function of the radius is measured via image analysis, showing a damage maximum at the specimen center that decreases toward the specimen border. This distribution was found to be consistent with that of the stress triaxiality ratio.



1. INTRODUCTION

Assessing the durability of engineering structures made of technical polymers is an increasing challenge nowadays. Scientific approaches for this subject fall into two categories. One is macroscopic, where global variables such as engineering stress and strain are used. The other is based on the micromechanical theory which considers the material deformation and damage micromechanisms. The latter approach requires a link between the mechanical properties and the microstructure evolution. Most of polymeric materials studies are based on uniaxial tests, using smooth specimen where necking appears in a location that cannot be controlled. When necking appears, the specimen is still subjected to uniaxial loading, but this geometrical irregularity induces a multiaxial stress state within the net cross section of the sample. This multiaxial stress state consists of high levels of the hydrostatic stress, to which polymers are reported to be sensitive.^{1,2}

Many microscopic examinations of the deformed microstructure of polymers exhibit voiding, which induces volume change within the material. Volume change on polymers was also a significant subject that was studied essentially at the macroscopic scale. Very few studies made a link between this volume change and the hydrostatic stress.^{3,4} The motivation of this work is to assess both change in shape and distribution of voids (volume change) by using X-ray tomography as a new observation technique, within a specimen geometry where the hydrostatic stress (stress triaxiality) is well controlled.^{5–7}

Previous work⁸ showed that X-ray tomography inspections of the necked region of a specimen from uniaxial tests on a polyamide 6 (PA6) exhibited a specific microstructure. This

consists of cavities arranged in columns and separated by thin walls of matter. This peculiar morphology together with its radial distribution could also be reproduced even in creep tests. The same PA6 semicrystalline polymer was then selected as model material because it is well suited to the resolution of the X-ray tomography. Additionally, the use of notched specimens allows a better control of the location of necking as well as to enhance void growth, which, accordingly, eases the process of quantifying the void volume fraction by image analysis. The same experimental techniques were used in a comprehensive examination campaign^{9,10} for poly(vinylidene fluoride) (PVF2) material. However, due to lower resolution and the nature of the PVF2 polymer, the details of void shape could not be accessed. Following the same methodology, the goal here was to carry out both ex-situ and in-situ tensile tests to follow the evolution of the microstructure. This paper focuses on the void shape and attempts to yield the profile of the void volume fraction within a notched geometry. The first part of the paper presents the experimental techniques and procedures. Results of the microstructure inspections are then presented in terms of void morphology and distributions within the sample. Prior to the concluding remarks, discussions take place about the advantages of the present experimental technique, the modeling in terms of true stress and strain tensors as it is reported in the literature, and the damage scenario supported by the experimental data collected in the previous sections.

Received: March 14, 2012

Revised: May 15, 2012

2. EXPERIMENTAL PROCEDURE

2.1. Interrupted Tests. The polyamide 6 (PA6) under study is a semicrystalline polymer for which physicochemical properties were

Table 1. Physicochemical Characteristic of the Polyamide 6 under Study

glass transition temperature, T_g	53 °C
degree of crystallinity	43%
spherulite mean diameter	5 μm
initial void volume fraction	1.5%
initial void mean diameter	0.1 μm

published elsewhere⁸ and are summarized in Table 1. The specimens had a gage section diameter of 7.2 mm and a gage length of 65 mm. The net (minimal) section diameter was 3.5 mm, whereas the notch root radius ρ was 4 mm. Cylindrical coordinates will be used all along

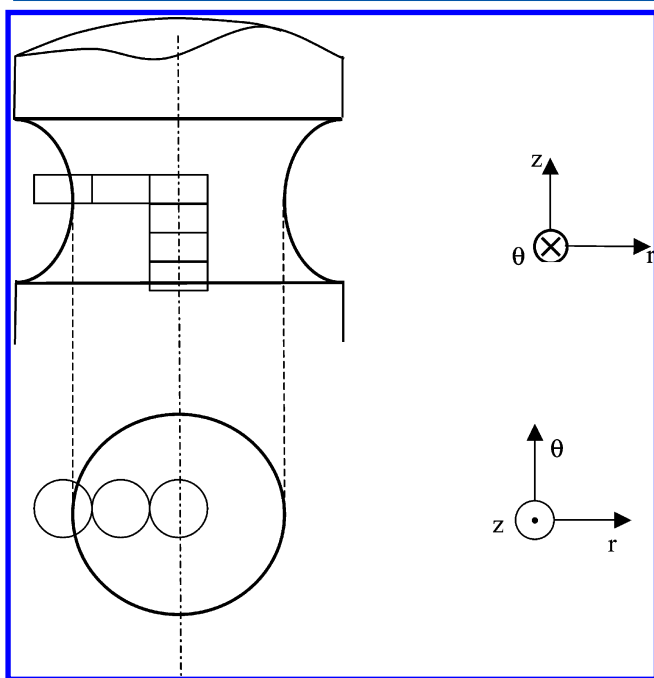


Figure 1. Local tomography: locations of the volumes of interest (VOI) as cylindrical stacks.

the paper as illustrated in Figure 1: the z -axis coincides with the tensile direction of the load, whereas the $(r\theta)$ plane corresponds to its cross section. The initial notch root radius induces triaxial stress state within the net section characterized by the initial stress triaxiality ratio T :¹¹

$$T = \frac{\sigma_m}{\sigma_{eq}} = \frac{1}{3} + \ln\left(1 + \frac{a^2 - r^2}{2aR}\right) \quad (1)$$

where r is the distance from the center of the net section, σ_m is the hydrostatic stress, σ_{eq} is the equivalent stress, a and R are respectively the net section and the notch root radii, and \ln is the naeperian logarithm.

The stress/strain tensors depend on the location of the point of interest and on the characteristic dimensions of the specimen:¹¹

$$\frac{\sigma_{\theta\theta}}{\sigma_{eq}} = \ln\left(1 + \frac{a^2 - r^2}{2aR}\right) \quad (2)$$

$$\frac{\sigma_{zz}}{\sigma_{eq}} = 1 + \ln\left(1 + \frac{a^2 - r^2}{2aR}\right) \quad (3)$$

Equations 2 and 3 give, in a cylindrical coordinate system (Figure 1), the expressions of the hoop and axial stresses, respectively, normalized by the equivalent stress as a function of the current radius within the net section. Strains are assumed to be homogeneous within the cross section. They can be approximated by¹¹

$$\epsilon_{zz} = \epsilon_{eq} \quad \text{and} \quad \epsilon_{rr} = \epsilon_{\theta\theta} = -(1/2)\epsilon_{zz} \quad (4)$$

A series of interrupted tests were carried out on notched specimens. Tensile tests were performed on an electromechanical tensile rig, monitoring both axial load and crosshead displacement during the test. The net stress was defined as the load divided by the initial net section area. Both net stress and crosshead displacement (in mm) will be used

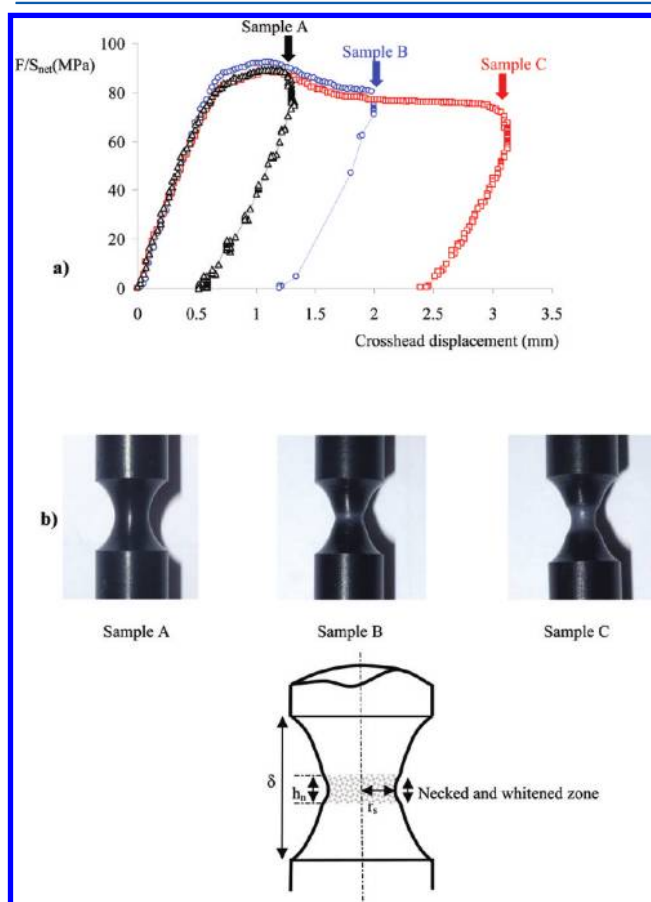


Figure 2. Experimental preparation of the PA6 notched samples: (a) sequence of loading path; (b) samples A, B, and C differ in the stretch of the whitened zone; (c) nomenclature of characteristic dimensions of a deformed specimen (Table 2).

as global or macroscopic parameters. Figure 2a describes that each test was stopped at a characteristic event of the stress–strain curve: at peak stress (sample A), after the postyielding stress decrease (sample B) and at the end of the plateau prior to final rupture (sample C). These events were based upon the stress–strain curve trends as it is classically observed at the macroscopic level. After unloading and specimen removal, samples were first photographed to record the deformed shape of the notched zone (Figure 2b) and then scanned 2 months later using X-ray tomography. The PA6 being known to exhibit non linear time dependent deformation (highly viscoplastic), these ex-situ tests attempted to inspect the voiding of the sample when the deformation is assumed to be permanent.

Some characteristic dimensions of the deformed samples are useful in the next analyses. The nominal diameter Φ remains approximately unchanged during the test. Therefore, the net section radius r_s , the axial notch opening (distance between both notch shoulders) δ , and the height h_n of whitened necking zone as depicted in Figure 2c were

Table 2. Characteristic Measures (All Values in mm) on Deformed Samples

	sample A	sample B	sample C
permanent set at zero stress after unloading	0.10	0.24	0.48
deformed net section r_s	1.69	1.38	1.16
half-deformed notch opening $\delta/2$	3.60	3.90	4.43
half-height of necking (whitened) zone $h_n/2$		0.32	1.38

measured. Table 2 summarizes these latter values together with the permanent set after the unloading, when the stress was zero. It can be noted that the net section diameter and the notch opening continuously decreases and increases respectively when the applied displacement increases. Additionally, the deformation is essentially localized within the net section, which appears whitened except for sample A.

An additional in-situ test was conducted in order to assess the analyzed void micromechanisms detected from ex-situ tests. In-situ test rig consisted of a simple screw driven load frame allowing incremental loading of the sample.¹² To this end, a small specimen was machined with a nominal diameter of 3.5 mm, a net section diameter of 2 mm, and a notch root radius of 0.5 mm. The specimen was loaded to 180 N and then scanned under load. The scan began after waiting 5 min, allowing the short-term stress relaxation. The associated flow of the material under load due to viscoplasticity slightly altered the image quality.

2.2. Synchrotron Radiation Tomography Technique Setup.

Synchrotron radiation tomography (SRT) was carried out by using the ID19 tomograph at the European Synchrotron Radiation Facility (ESRF) in Grenoble, France. The tomographic setup used a monochromatic parallel beam tuned at 17.6 keV going through the sample to the scintillator. Attenuated X-rays are then transformed into visible light which is collected by a 1024 × 512 pixels restricted zone of the Frelon CCD camera to form a radiograph. A tomographic scan corresponded to a set of 1500 radiographs, recorded continuously over a 180° rotation. Exposure time was set to 0.1 s, resulting in scan duration of 3 min. This value was found to be appropriate, especially for in-situ scans where long exposure may heat the sample and alter the microstructure. The distance between the specimen and the camera was set to 25 mm which lead to a combination of absorption and phase contrast helping to highlight voids present inside the sample.¹³ The size of the isotropic voxels in the reconstructed volumes was 0.7 μm . In this setup the material volume contributing to the projection had a diameter of about 3 mm while the width of the field of view (hence the diameter of the maximum reconstructed 3D volume) was only of 716 μm (and its height 358 μm). This setup condition where the sample is larger than the detector's field of view is also called "local tomography" and has been used for instance by Youssef et al.¹⁴ Its main interest is to avoid a tedious cutting of the sample (that would otherwise be requested to adapt to the imaging setup). In the particular case of the low absorbent rather homogeneous material of the present study, the local tomography condition provided reconstructed images of sufficient quality.

Figure 1 describes the locations of the cylindrical volumes (height 358 μm , diameter 716 μm) imaged by SRT—noted also volumes of interest (VOI)—obtained during the analysis. The locations of VOI are illustrated as open circles in the cross section (r, θ) view and as open rectangles in the longitudinal (r, z) view, respectively. Each SRT image in 2D is accompanied by this illustration to indicate the position of the VOI in the notched area. Experimentally, acquisition in these

different locations is obtained by physically displacing the sample in space. In practice, the center of the neck is first positioned in the field of view of the detector using radiography inspection, and the scan is acquired. The sample is then displaced along y - or z -axes for radial and axial displacements, respectively, before acquiring the scans in another location. Finally, the acquired data sets consist of about 7 and 4 scans along z - and r -directions, respectively (Figure 1).

2.3. Evaluation of Void Volume Fraction by Image Processing. For each sample, the various scans were assembled into one large virtual image. The void volume fraction (V_f) was computed using image processing along both the radial and the axial directions.

To this end, small parallelepipedic volume^b of about $170 \times 170 \times 120 \mu\text{m}^3$ was sampled from the large virtual data set. Each measure V_f is registered then into the deformed specimen coordinates system (see Table 2).

To retrieve the void volume fraction, gray level images are first segmented using watershed contour detection. Each void is then identified thanks to gray level thresholding using local minima.^{15,16} With this method, morphological parameters such as characteristic lengths, volume, and angle with respect to the loading direction can be extracted in 3D on each void. Nevertheless, due to space constraints, the present work focuses only on the void volume fraction distribution, which is the first parameter calculated in most of the papers in the literature.^{9,10} These data are significantly useful for damage mechanics modeling. Indeed, the V_f distribution turns out to be necessary to calibrate damage coefficients in a damage based model such as published by Boisset et al.⁴

3. SRT INSPECTION RESULTS

3.1. Morphology of Voids. This section is devoted to describe qualitatively voids formed during deformation using the shape factor as well as looking at the clustering effects, with respect to the strain level reached within the sample (A, B, or C).

Figure 3 shows reconstructed slices extracted from a VOI located near the notch root (surface). These pictures are equivalent to the classical 2D images for microstructure observations (for instance, SEM observations after microtome cutting). In the following, the samples of interest consist of volumes whose dimensions were either ($140 \mu\text{m} \times 140 \mu\text{m} \times 140 \mu\text{m}$) or ($350 \mu\text{m} \times 140 \mu\text{m} \times 140 \mu\text{m}$) extracted from each sample in Figure 2. Images are presented in perspective to better reveal the 3D effects. Evolution of the morphology in time and space is then highlighted.

In the Center of the VOI. Figure 4a shows the cube corresponding to the sample stopped at the peak stress. According to Figure 1b (sample A), no apparent deformation/whitening was detected at the macroscopic scale. From the top view ($r\theta$ cut), voids are round-shaped, whereas in the longitudinal cut (rz plane), their morphology is similar to what can be identified as craze.^{17–19} Indeed, within the apparent penny-shaped cracks, residual ligaments of matter (fibrils) can be seen from the top view. This description (cavitation + fibrils) is consistent with that reported by Plummer et al.²⁰ in their comprehensive study of craze nucleation. Multiple crazes, perpendicular to the load direction, are observed within the microstructure leading to a pileup of many crazes in some places.

Figure 4b is dedicated to sample B for which the test was stopped just after the stress decrease. Figure 1b showed that the sample underwent necking with a short whitened zone. Void aspects are similar to that of Figure 4a, but their height increased, as the height of whitened zone observed macroscopically (Figure 1b: sample B). Moreover, columns of voids can be distinguished emanating from pile ups of crazes initially

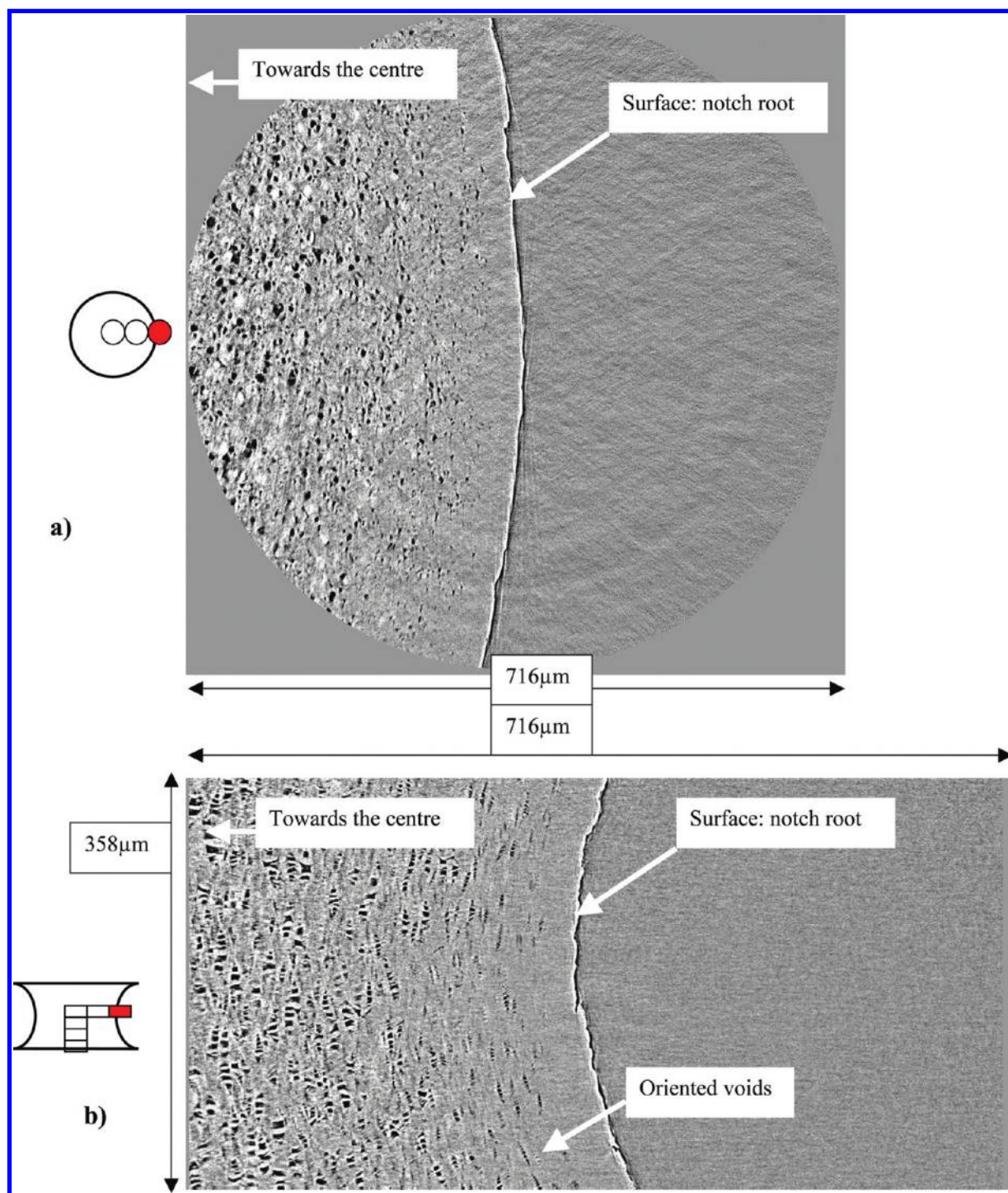


Figure 3. Sample B, morphology of voids within the minimal cross section $z = 0$, $r = a$: (a) top view ($r\theta$) of the net cross section ($716 \mu\text{m}$)²; (b) view through longitudinal cut (rz) ($716 \mu\text{m} \times 538 \mu\text{m}$).

aligned parallel to the tensile direction. In the longitudinal cut (rz cut), porosity appears cylindrical in the middle and conical at the ends of the column, separated by thin layers of material (in white).

Similar void column shapes were observed on initially smooth specimen that underwent necking.⁸ This feature was also observed and analyzed by Pawlak and Galeski^{21,22} in polypropylene tested under uniaxial tension and subjected to necking. According to these authors, “polar fans” within the spherulitic microstructure were the origin of this peculiar

morphology. In the present SRT inspection, spherulites boundaries could not be observed so the location of the void columns within the spherulites could not be established. From sample A to sample B, the mean diameter of crazes seems to be constant. Therefore, the opening of the craze structure essentially consists of volume change. The stress softening observed at the macroscopic scale is actually related to a significant volume change within the necked zone.

Figure 4c shows the microstructure at the end of the test after a significant neck extension in the z direction (see Figure

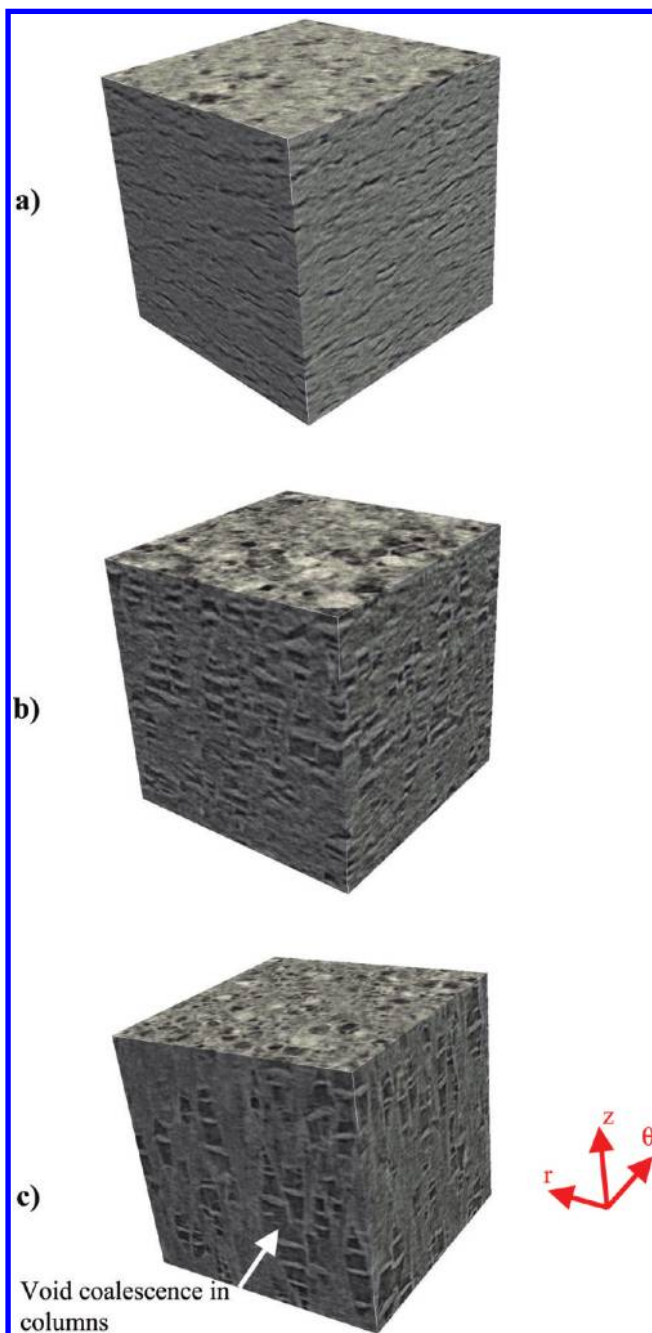


Figure 4. 3D representation of a $140\ \mu\text{m} \times 140\ \mu\text{m} \times 140\ \mu\text{m}$ cubes extracted from the VOI in the center of each sample: (a) sample A at the peak stress; (b) sample B, just after the stress softening; (c) sample C, prior to the final rupture.

2b: sample C). The same volumetric transformation as in Figure 4b is observed (increase in cylindrical void height). The contours of void columns are more precise due to lateral walls becoming thinner (appear in white). This observation is consistent with the previous work on the same PA6.⁸ The only difference was in the value of the mean diameter of voids: in the present work it is twice bigger than that of the initially smooth (un-notched) specimen. The increase in mean diameter of the initial craze is due to the presence of the initial notch radius and hence to the higher stress triaxiality as expressed in eq 1. In Figure 4c, some places showed that the walls (horizontal matter

ligaments between voids) were broken resulting in a coalescence in column.

Another specificity of sample C examination was the presence of several big cavities within the VOI. Attention was paid to the largest cavity (diameter $\sim 100\ \mu\text{m}$) in Figure 5. Figures 5a,b show details in 2D of this cavity and indicate its location within the VOI. The 3D image of Figure 5c shows that the big cavity results from the radial coalescence of initially individual void columns. The final failure of the specimen can then be attributed to a radial coalescence of void columns. This was also detected at the macroscopic scale by the load drop just before the test arrest (Figure 2a). Similar failure mechanisms initiating from few macrocavities were reported concerning PVF2 material.^{9,10}

In the Vicinity of the Notch Root (Surface). Figure 3 recalls 2D images for sample B where specific void columns morphology is evidenced. When approaching the notch root surface, an orientation effect of void columns was observed. In this section, 3D pieces of material ($350\ \mu\text{m} \times 140\ \mu\text{m} \times 140\ \mu\text{m}$) extracted from the notch root of each sample are analyzed. For the sake of clarity, specific orientation and location were indicated according to each piece of material in Figure 6.

In Figure 6a, sample A exhibits a gradient in void number per volume unit as well as in void mean diameter along the r -axis. The morphology remains like penny-shaped crazes. Figure 6b corresponding to the sample B shows the same morphology as in Figure 4b. Following 2D sections in Figure 3, void columns near the notch root are oriented, according to the notch root shape. This orientation could be observed for this specific sample where the extension of the neck was not so significant (see Figure 1b, sample B). Actually, the notch root profile remained curved in this case. Since void columns in the center were observed to be parallel to the load direction (z -axis), a gradient of orientation is revealed here. This orientation effect is of prime importance from the mechanical viewpoint.

Figure 6c shows the same trends as Figure 5b, except for the orientation of void columns near the notch root. In fact, the notch root was no longer “curve shaped” at this stage of the loading due to the extension of the neck. It can be summarized that for increasing r both void diameter and number decrease.

In the Vicinity of the Neck Shoulder (Center). The aforementioned observations were carried out at three distinct events during the loading conditions. It was noticed that for sample C void morphology changed along the z -axis, especially around the neck shoulder. Figure 7 illustrates this effect. Near the top surface, voids are aligned in columns. Then, the microstructure gradually evolves to reveal multicrazes when approaching the neck shoulder. Void morphology close to the neck shoulder for sample B is similar to that of sample A arrested at the peak stress (Figure 4a, sample A). From then on, the morphology gradient with respect to z -axis can be assimilated to that occurring in the center for increasing load. It can be summarized that for increasing z the mean void height decreases, which is also the case for voids at a given location for increasing load.

In-Situ versus Interrupted Tests. In the previous subsections results were showed for samples issued from interrupted tests. After unloading, permanent displacements of 0.1, 0.25, and 0.5 mm were experimentally observed (Figure 2). In order to make sure that the morphology of voids was not affected by the unloading sequence, in-situ test as described in section 2 was carried out. Because of space constraint, only comparison between images at peak stress was made here. Figure 8

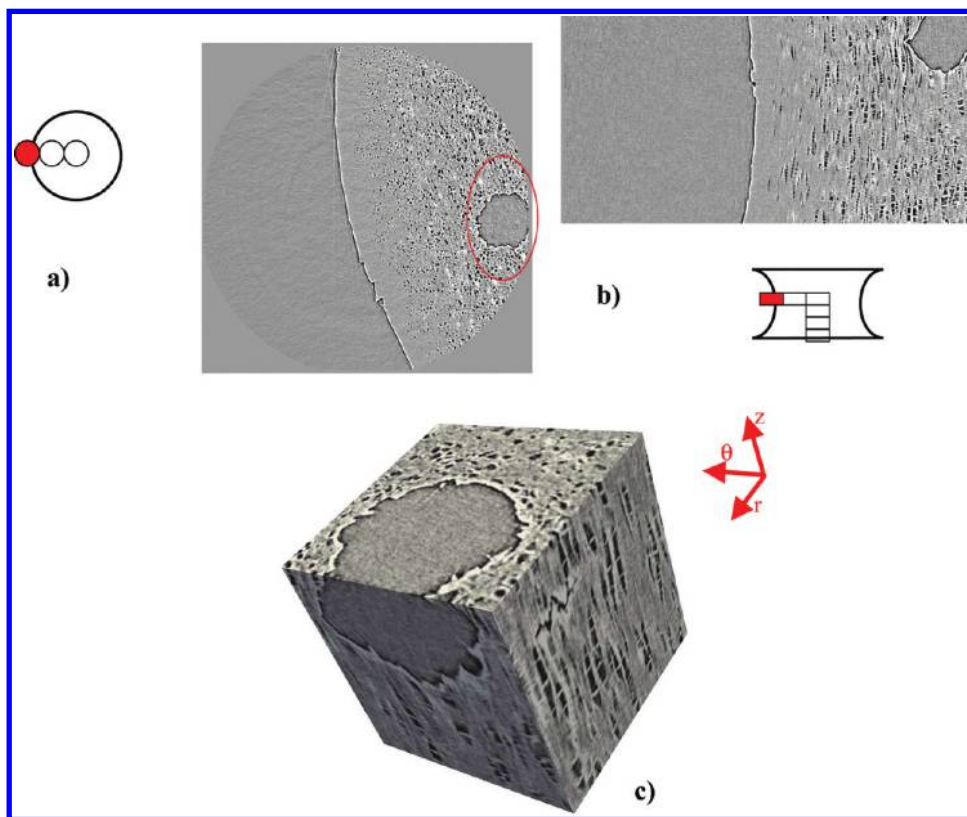


Figure 5. Sample C, morphology of voids in the net cross section ($z = 0$, $0 < r \leq a$): (a, b) views and location of the $100 \mu\text{m}$ cavity; (c) details in 3D $(140 \mu\text{m})^3$ of the microstructure around the big cavity.

describes the morphology of voids near the center of specimen by comparing in-situ with ex-situ (sample A) tests. Scans during in-situ tests are subjected to some artifacts, essentially due to the stress relaxation and to higher phase contrast level caused by the presence of the in-situ tensile rig. Nevertheless, Figure 8 clearly shows that the morphology of crazes in both cases is very similar. This demonstrates that there is no major effect of the unloading sequence in interrupted tests in terms of void morphology.

3.2. Space Distributions of Void Volume Fraction V_f .

The previous subsections were devoted to a qualitative description of voids, although a gradient of the porosity was invoked. Before going further, it should be reminded that V_f determination is affected by uncertainties due to the experimental technique. The fine resolution of about $0.7 \mu\text{m}$ here can be considered as a lower limit of the detection of voids. Indeed, for the PA6 of interest, the initial porosity was measured thanks to the inspection of cryo-fractured surfaces.⁸ Initial void volume fraction was then estimated at 1.5% with void mean diameter of $0.1 \mu\text{m}$. Of course, this could not be accounted for in the present determination of V_f . The following analyses display V_f as determined by the image analysis routine (see section 2.3). The precision on absolute V_f values being dependent on the image processing methodology,^{9,10} these values are still subject to caution. The discussion rather focuses on the trends which appear very reliable. To this end, V_f is systematically normalized by the maximum value ($V_{f_{\max}}$) obtained in the center of the net cross section for the corresponding sample.

Additionally, uncertainties on the exact position of the parallelepiped barycenter in terms of r and z were also encountered. Although a great effort was made to center the

sample during the SRT scan, the precision in positioning the center of the sample were estimated around 0.1 mm .

Radial Distributions. Radial distributions of the normalized void volume fraction were plotted within the net section in Figure 9. The current radius r is normalized by the net section radius r_s (Table 2), obviously represented in the deformed state. The vertical dashed line ($r = 0$) approximately symbolizes the sample axis (center of the net section). Whereas for samples B and C (Figures 3 and 6), scans near the surface included the notch root, sample A scans did not reach the notch root surface due to the larger diameter of the net section ($r_s = 1.69 \text{ mm}$).

For all samples, $V_{f_{\max}}$ is located in the center of the net section. In the vicinity of the notch root surface, Figures 3 and 6 clearly indicate that no voiding appeared in a thin layer of material. At this location a small value of V_f is observed due to the averaging operation of V_f . Parallelepipeds near the surface were finely sampled. $V_{f_{\max}}$ increases with the load applied to the sample. Reported values are 11%, 15%, and 16% for sample A, B, and C, respectively. For sample A, a smooth gradient of V_f is observed from the center to the surface. Samples B and C exhibit larger plateau than sample A in the center, followed by a steep slope near the surface. According to Figures 4, 6, and 8, sample A exhibits penny shaped multicrazes, whereas samples B and C showed fewer voids per volume unit with greater height/volume. This change in morphology cannot be characterized by the void volume fraction parameter.

In order to link the microstructural parameter V_f to a mechanical one, the stress triaxiality ratio T (eq 1) is selected. Indeed, according to Bridgman relationship, T is the mechanical parameter that can be related to V_f . In Figure 9, the solid line plots T superimposed to the radial distribution of voids. It can clearly be observed that the shape of the curves is

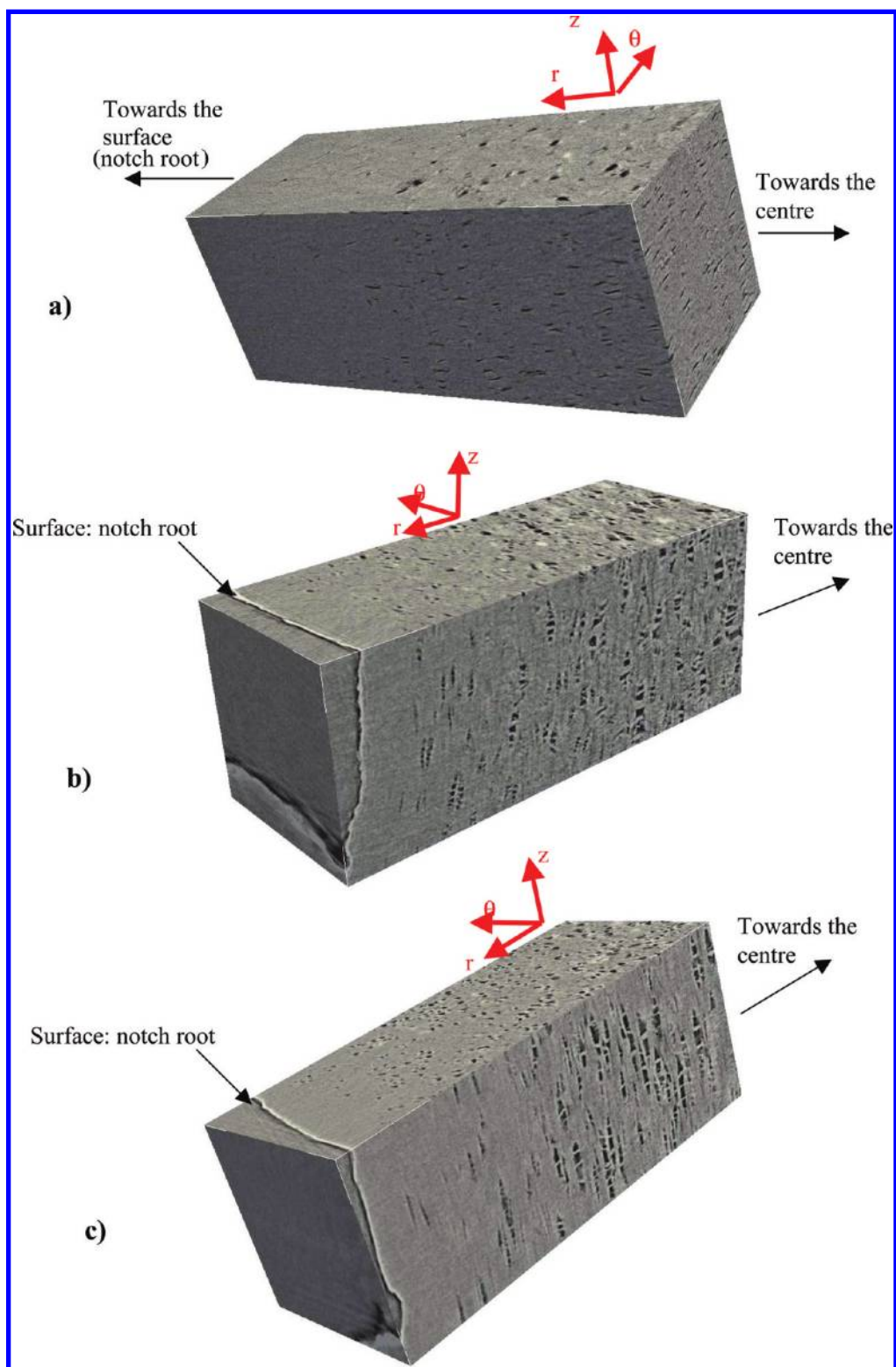


Figure 6. 3D representation of a $350\ \mu\text{m} \times 140\ \mu\text{m} \times 140\ \mu\text{m}$ piece extracted from the VOI near the notch root: (a) sample A at the peak stress; (b) sample B, just after the stress softening; (c) sample C, prior to the final rupture.

in good agreement in that their maxima are both located in the center of the net section. Additionally, this shape is similar to that of the axial or hoop stresses as expressed in eqs 2 and 3. This gradient of V_f within the net section, already encountered in metallic materials, was also reported for polymers.^{4,5,9} These data were of prime importance to the construction of damage-based models..

Axial Distributions. The axial distribution is essentially based on Figure 7 where voids are almost cylindrical (height \geq diameter) around the net section and gradually adopt a penny shape when z increases. As mentioned previously, only the void volume fraction gradient was quantified; void shape factors and anisotropy will not be discussed here. In Figure 10, the z in the deformed state was normalized by $\delta/2$ (see Table 2). The

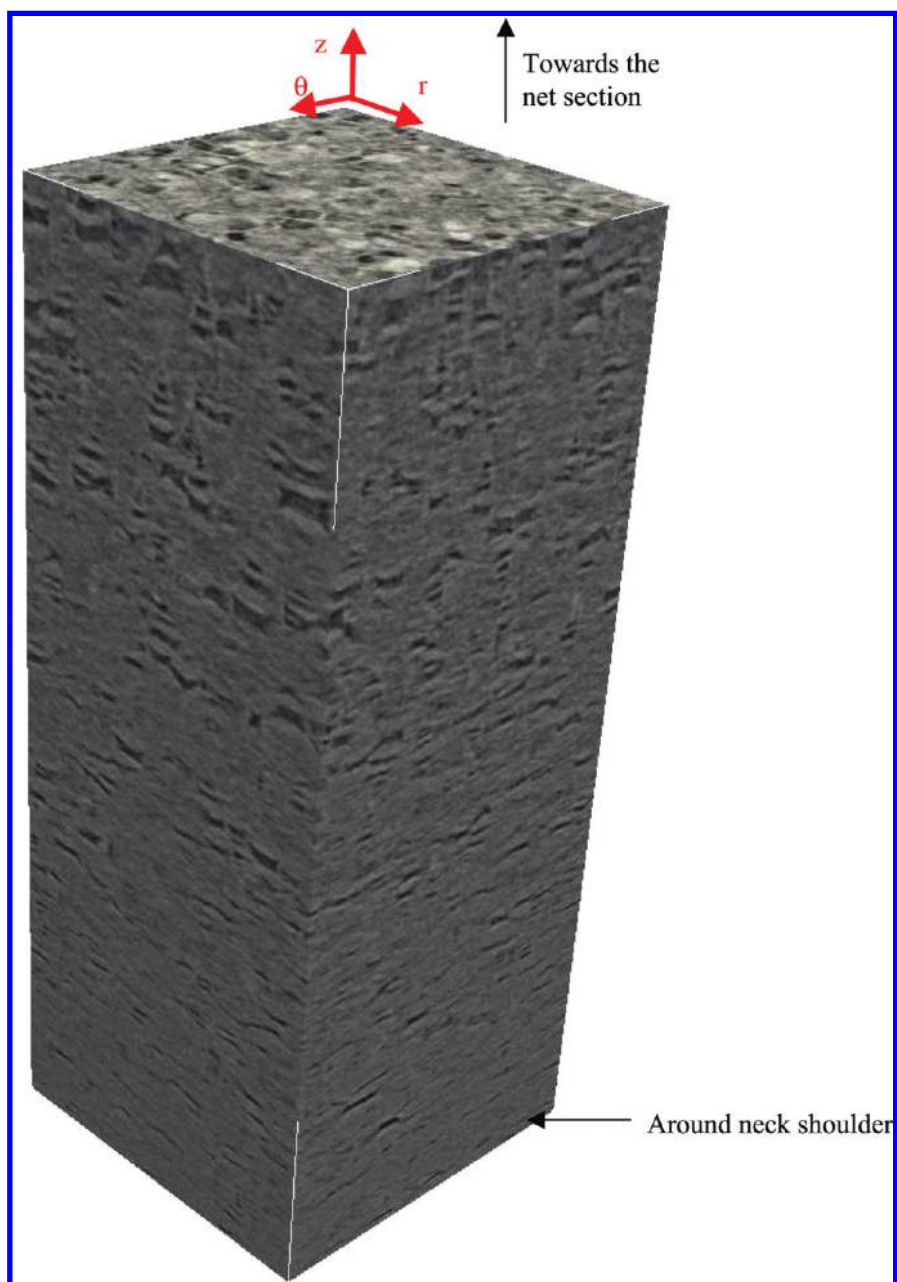


Figure 7. 3D representation of a $140\ \mu\text{m} \times 140\ \mu\text{m} \times 350\ \mu\text{m}$ piece extracted from the VOI near the notch shoulder. Axial decrease in void volume fraction, void mean height.

vertical dashed line ($z = 0$) approximately symbolizes the net cross section of the sample. It can be observed that the maximum of V_f is located near the net section. The change in the void morphology (cylindrical to penny shaped) regarding the axial distribution was observed in samples B and C. Once again, the void volume fraction parameter cannot characterize this change in morphology. For sample A voids are entirely penny shaped, and it is interesting to notice that the transition between the two morphologies of voids operates around $V_{f_{\max}}$ of sample A ($\sim 10\%$). For larger V_f in samples B and C, a relative plateau can be observed near the net section, but it was not so pronounced as in the radial distribution. It was also noticed that the drop of V_f coincided with h_n the half-height of the whitened (necking) zones (Table 2) at the macroscopic level. Similar results were reported on PVF2,^{9,10} demonstrating

that these phenomena are likely to appear in many semicrystalline polymers.

Following the same approach as in the radial direction, the axial distribution of T was approximated by Beremin²³ formula obtained by extension of eq 1 and expressed as follows, for $r = 0$:

$$T = \frac{\sigma_m}{\sigma_{eq}} \approx \frac{1}{3} + \left(1 - 2\left(\frac{z}{a}\right)^2\right) \ln\left(1 + \frac{a}{2R}\right) \quad (5)$$

In Figure 10, the V_f distribution is compared again with that of the stress triaxiality ratio as a function of normalized z (solid line). Good agreement is obtained between the void distribution and T profile. It is worth noting that such a comparison is very seldom if ever made in the literature

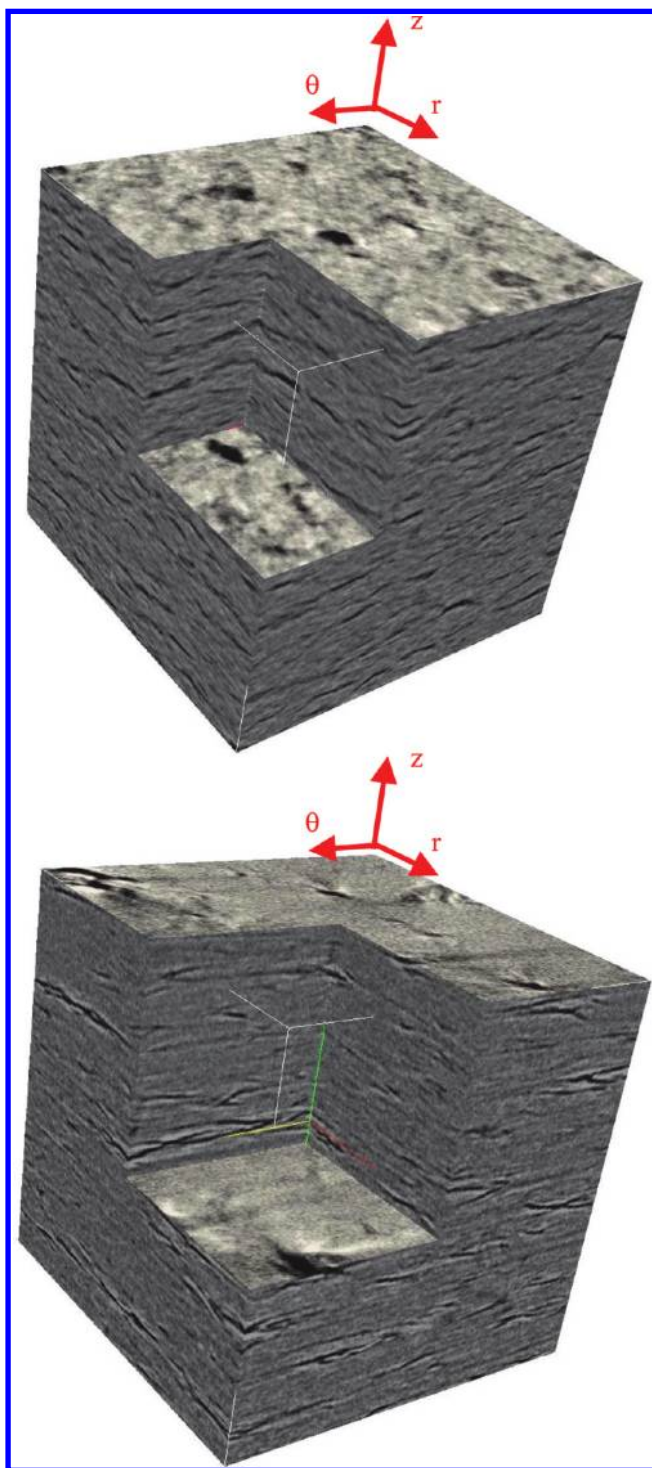


Figure 8. Comparison between morphology of voids: (a) sample A from ex-situ test stopped at the peak stress; (b) sample from in situ test ($140\ \mu\text{m} \times 140\ \mu\text{m} \times 140\ \mu\text{m}$ cube).

although these results are of prime importance for damage-based material modeling.

4. DISCUSSIONS: MECHANISMS OF DAMAGE EVOLUTION

4.1. Experimental Techniques. Studies devoted to cold drawing of polymers generally investigate the necking in terms of deformation micromechanisms without taking the multiaxial stress state into account. The classical observation techniques

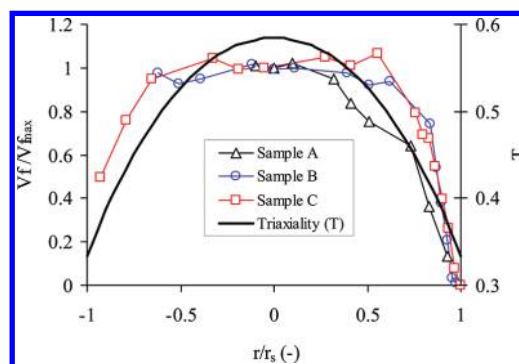


Figure 9. Trends of radial distributions of void volume fraction (V_f) normalized by corresponding $V_{f_{\max}}$ in the vicinity of the net section for each sample ($V_{f_{\max}} = 11\%$, 15% , and 16% respectively for sample A, B, and C). In solid line (second Y-axis), the triaxiality profile according to eq 1 for NT4 specimen.

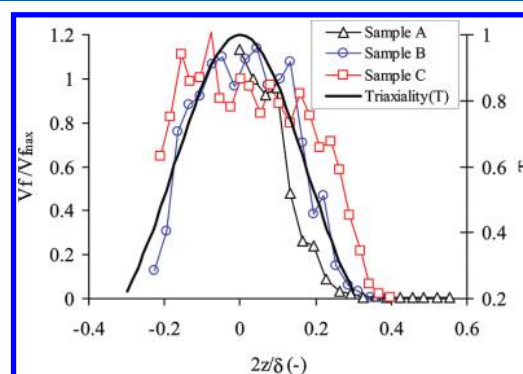


Figure 10. Trends of axial distributions of void volume fraction (V_f) normalized by corresponding $V_{f_{\max}}$ in the vicinity of the whitened area for each sample ($V_{f_{\max}} = 11\%$, 15% , and 16% respectively for sample A, B, and C). In solid line (second Y-axis), the triaxiality profile according to eqs 2 and 3 for the NT4 specimen.

used were small- and wide-angle X-ray scattering (SAXS and WAXS, respectively). Blaise et al.²⁴ used the incoherent polarized steady-light transport (IPSLT)^{25,26} technique to follow cavitation of polyethylene. These experimental techniques generally give the average value of the porosity in the whole VOI, but a precise spatial distribution of void could not be determined. Even in the work of Rosenberg et al.⁹ dedicated to the study of cavitation of poly(vinyl fluoride) (PVF2) by the SRT technique, the authors reported that voids were “quantified as a whole” due to a poor resolution. In addition, classical scanning/transmission electron microscopy (SEM, TEM) techniques can give a 2D distribution.^{4,18,20} However, long preparation of the sample (microtome, cryofracture) is needed for these latter techniques. The present paper highlights the ability of SRT technique to deliver valuable 3D data that can serve as input for full field finite element simulations.

4.2. Hydrostatic Pressure versus Volume Change Relationship. The true stress and strain fields within a notched body were modeled here by using the approximate formulas proposed by Bridgman,¹¹ Kachanov,²⁷ extended by Beremin.²³ In the work of Boissot et al.,⁴ for polyamide 11 material, void radial distribution within the necked specimens were SEM observed from microtomed cut samples from interrupted tests. The stress and strain distributions could be modeled by Beremin formulas²³ up to the peak stress. In the present work, this model can be applied only to sample A and

for the in-situ test (Figures 9 and 10). For samples B and C, the increase in V_f is such that a parameter related to the significant volume change is needed. Therefore, FE computation with a damage based constitutive relationships is required. Investigation carried out by Boisot et al.⁴ in this way leads to the following conclusions: (i) void growth simulation induced heterogeneous volume change within the VOI; (ii) V_f radial distributions were consistent with the largest principal stress gradient by opposition to the largest principal strain; (iii) the relationship between the hydrostatic pressure and the volume change depends on the void volume fraction.

Current works on FE modeling of the PA6 under study lead to the same conclusions.

4.3. Damage Mechanics Scenario. Unlike other existing techniques such as IPSLT^{25,26} or X-ray scattering,^{28,29} the main advantage of SRT technique is to actually be able to visualize in 3D the voids. A scenario for void growth can be proposed consisting of outgrowth (radial expansion) of voids perpendicularly to the load direction, prior to axial elongation (stretching). Indeed, before the peak load, penny-shaped crazes²⁸ form, inducing anisotropy perpendicular to the load direction. Then, crazes transform to crack (breakage of the residual ligaments), in turn forming void columns and inducing anisotropy following the load direction. This ascertains many reports^{24,30} indicating that anisotropy of voids evolves first perpendicularly to the direction of loading (radial expansion of voids = crazes) then rotates to end by following the loading direction. Similar observations coming from SAXS and WAXS techniques were published by Humbert et al.²⁸ and Castagnet et al.³¹

5. CONCLUSION

SRT observations on the necking area of a PA6 initially smooth specimen⁸ showed voids aligned in the tensile direction and separated by thin ligaments of matter. To better understand the mechanisms leading to this morphology, tensile tests on initially notched specimens were carried out. A notch root radius of 4 mm was implanted in the specimen because this geometry was sufficiently well studied in the literature to allow a better control of the multiaxial stress state within the notched region. Ex-situ tests were arrested (i) at peak load; (ii) at the end of the load decrease; (iii) at the onset of the final failure, to observe the microstructure changes at these specific steps of the loading. Moreover, an in-situ test was performed on smaller also notched specimen up to the peak load demonstrating that the void morphology at this stage was not affected by the unloading sequence for interrupted tests.

Voids were observed as penny-shaped crazes at the peak load in the specimen center and after peak load near the neck shoulders. This morphology prevails before the extension of the necking during which voids become cylindrical in the middle of the characteristic void column and conical at both ends. The transformation was observed to consist essentially of a volume change. Void columns appear after the load decrease and extend in height all along the plateau of the stress–strain curve. As expected, the mean diameter of crazes/voids in initially notched specimens was bigger than that of initially smooth—say uniaxial—specimens. The final failure of the specimen is provoked by the coalescence of void columns.

Quantification of the void volume fraction (V_f) was attempted by using an original image analysis software based on mathematical morphology concepts. Radial distribution of voids showed that the maximum V_f was systematically located

in the center of the specimen, where the stress triaxiality ratio is maximum. Of course, this maximum value increases with the loading. The V_f radial distribution is parabolic at the peak load, but the necking extension modifies this profile to a plateau in the central region followed by a strong decrease near the notch surface. Axial distribution shows a maximum value at the net section ($z = 0$) and a decrease when away from this plane ($z > 0$).

The SRT technique was shown to be useful for describing the microstructure evolution when the studied material damage features are adapted to the achievable resolution. Unlike other experimental techniques, this one is nondestructive and allows 3D observations (so properties gradient within the volume) that involve deformation induced anisotropy (orientation). The distribution of void volume fraction is in agreement with the stress triaxiality profile, whereas the orientation of void columns was found to be consistent with that of the largest principal stress. It can then be concluded that the true stress tensor is the key parameter that controls the damage evolution.

AUTHOR INFORMATION

Corresponding Author

*Tel +33-1-60-76-30-64, Fax +33-1-60-76-31-50, e-mail lucien.laiarinandrasana@mines-paristech.fr.

Notes

The authors declare no competing financial interest.

ACKNOWLEDGMENTS

We are indebted to Wolfgang Ludwig for helping us conducting the experiments at ESRF. Deep thanks to Julie Heurtel for technical assistance and to Ian Sinclair from University of Southampton for providing the tensile rig.

ADDITIONAL NOTES

^aThe number of scans slightly differs from sample to sample. For instance, only half of the radial direction was imaged for sample A.

^bOn the edge of the samples, the volume size is decreased down to $40 \times 40 \times 120 \mu\text{m}^3$ to capture the stronger gradient of the void volume fraction.

REFERENCES

- (1) Sternstein, S. S.; Myers, F. A. J. *Macromol. Sci., Part B: Phys.* **1973**, *8*, 539–571.
- (2) Moonan, W. K.; Tschoegl, N. W. J. *Polym. Sci., Polym. Phys. Ed.* **1985**, *23* (4), 623–651.
- (3) Ghorbel, E. *Int. J. Plast.* **2008**, *24*, 2032–2058.
- (4) Boisot, G.; Laiarinandrasana, L.; Besson, J.; Fond, C.; Hochstetter, G. *Int. J. Solids Struct.* **2011**, *48*, 2642–2654.
- (5) Challier, M.; Besson, J.; Laiarinandrasana, L.; Piques, R. *Eng. Fract. Mech.* **2006**, *73*, 79–90.
- (6) Laiarinandrasana, L.; Besson, J.; Lafarge, M.; Hochstetter, G. *Int. J. Plast.* **2009**, *25*, 1301–1324.
- (7) Castagnet, S.; Deburck, Y. *Mater. Sci. Eng., A* **2007**, *448*, 56–66.
- (8) Laiarinandrasana, L.; Morgeneyer, T. F.; Proudhon, H.; Regrain, C. J. *Polym. Sci., Part B: Polym. Phys.* **2010**, *48*, 1516–1525.
- (9) Rosenberg, E.; Brusselle-Dupend, N.; Epsztein, T. *Mater. Sci. Eng., A* **2011**, *528*, 6535–6544.
- (10) Brusselle-Dupend, N.; Rosenberg, E.; Adrien, J. *Mater. Sci. Eng., A* **2011**, *530*, 36–50.
- (11) Bridgman, P. W. In *Metallurgy and Metallurgical Engineering Series*, 1st ed., McGraw-Hill Book Co., Inc.: New York, 1952; pp 9–37.
- (12) Scott, A. E.; Mavrogordato, M.; Wright, P.; Sinclair, I.; Spearing, S. M. *Compos. Sci. Technol.* **2011**, *71*, 1471–1477.

- (13) Cloetens, P.; Pateyron-Salomé, M.; Buffière, J.-Y.; Peix, G.; Baruchel, J.; Peyrin, F.; Schlenker, M. *J. Appl. Phys.* **1997**, *81*, 5878–5886.
- (14) Youssef, S.; Maire, E.; Gaertner, R. *Acta Mater.* **2005**, *53* (3), 719–730.
- (15) Serrat, J. *Image Analysis and Mathematical Morphology*; Academic Press: London, 1988; Vol. 2.
- (16) Beucher, S. Thesis, Ecole Nationale Supérieure des Mines de Paris, 1990 (in French).
- (17) Kausch, H. H. *Polymer Fracture*, 2nd revised and enlarged ed.; Springer-Verlag: Berlin, 1987.
- (18) Grein, C.; Plummer, C. J. G.; Kausch, H. H.; Germain, Y.; Béguelin, Ph. *Polymer* **2002**, *43*, 3279–3293.
- (19) Henning, S.; Adhikari, R.; Michler, G. H.; Balta-Kalleja, S. J.; Karger-Kocsis, J. *Macromol. Symp.* **2004**, *214*, 157–171.
- (20) Plummer, C. J. G.; Goldberg, A.; Ghanem, A. *Polymer* **2001**, *42*, 9551–9564.
- (21) Pawlak, A.; Galeski, A. *Macromolecules* **2008**, *41*, 2839–2851.
- (22) Pawlak, A.; Galeski, A. *J. Polym. Sci., Part B: Polym. Phys.* **2010**, *48*, 1271–1280.
- (23) Beremin, F. M. *J. Mécanique Appliquée* **1980**, *4* (3), 307–325.
- (24) Blaise, A.; Baravian, C.; André, S.; Dillet, J.; Michot, L. J.; Mokso, R. *Macromolecules* **2010**, *43*, 8143–8152.
- (25) Schirrer, R.; Lenke, R.; Boudouaz. *Polym. Eng. Sci.* **1997**, *37* (10), 1748–1760.
- (26) Gehant, S.; Schirrer, R. *J. Polym. Sci., Part B: Polym. Phys.* **1998**, *37*, 113–126.
- (27) Kachanov, L. M. In *Fundamentals of the Theory of Plasticity*; MIR Publisher: Moscow, 1974; pp 292–294.
- (28) Humbert, S.; Lame, O.; Chenal, J. M.; Rochas, C.; Vigier, G. *Macromolecules* **2010**, *43*, 7212–7221.
- (29) Thomas, C.; Ferreira, V.; Coulon, G.; Seguela, R. *Polymer* **2007**, *48*, 6041–6048.
- (30) Butler, M. F.; Donald, A. M. *Macromolecules* **1998**, *31*, 6234–6249.
- (31) Castagnet, S.; Girault, S.; Gacougnolle, J. L.; Dang, P. *Polymer* **2000**, *41*, 7523–7530.